creased plasma density might occur, but they are probably insufficient to explain the observations. Inverse-Compton scattering of the GRP photons, kicking them up to the optical band, seems unlikely on several grounds, because only about 1% of the radio energy should appear as optical emission (*22*), whereas we find nearly equal luminosities. The γ-ray upper limit (*6*) also suggests no more than ≅1% conversion.

A consistent explanation is that the optical emission is a reflection of increased plasma density that causes the GRP event. Whatever triggers the GRP phenomenon, it releases energy uniformly throughout most of the electromagnetic spectrum, as implied by the similar energies of radio and enhanced optical pulses. Changes in the pair production rate at the level of a few percent could explain the optical variations and would also be expected at higher energies; existing limits to enhanced γ-ray emission (*6*) do not contradict this. However, an additional mechanism would be needed to account for the radio GRPs, which are orders of magnitude stronger than the average pulse level. It has been suggested (*24*) that this could be achieved by local density enhancements to the plasma stream, which increase the coherent emission ($\propto n^2$) with little effect on the (high-energy) incoherent radiation ($\propto n$). These changes must occur on tiny time scales (<10 μs) to explain the observed change in optical flux and the upper limit in the γ-ray region (*6, 23*). This result is also consistent with the recent observations of nanosecond time scale structure within GRPs (*24*). Whatever the mechanism, our observations demonstrate a clear link at the individual pulse level between the coherent and incoherent emission regimes in the Crab pulsar.

References and Notes

1. M. Lyutikov, R. D. Blandford, G. Machabeli, *Mon. Not. R. Astron. Soc.* **305**, 338L (1999).
2. Synchrotron and curvature radiation are produced when a charged particle moves in the vicinity of a magnetic field. Synchrotron radiation is produced when the particle follows a gyratory path around a magnetic field line, and curvature radiation is the limit when the particle follows a curved field line. See (*25*) for a detailed treatment.
3. A. K. Harding, J. K. Daugherty, *Adv. Space Res.* **21**, 251H (1998).
4. R. W. Romani, *Astrophys. J.* **470**, 469 (1996).
5. R. W. Romani, I.-A. Yadigaroglu, *Astrophys. J.* **438**, 314 (1995).
6. S. C. Lundgren, *et al.*, *Astrophys. J.* **453**, 433 (1995).
7. D. Hegyi, R. Novick, P. Thaddeus, *IAU Symposium* **46**, 129 (1971).
8. D. H. P. Jones, F. G. Smith, J. E. Nelson, *Nature* **283**, 50 (1980).
9. D. H. Staelin, E. C. Reifenstein, *Science* **162**, 1481 (1968).
10. I. Cognard, J. A. Shrauner, J. H. Taylor, S. E. Thorsett, *Astrophys. J.* **457**, L816 (1996).
11. R. W. Romani, S. Johnston, *Astrophys. J.* **557**, L93 (2001).
12. S. Johnston, R. W. Romani, *Astrophys. J.* **590**, L95 (2003); available at http://arxiv.org/abs/astro-ph/0305235.
13. The light cylinder is defined as the distance at which the corotation velocity equals the speed of light.
14. D. Buckton, O. Ryan, A. Shearer, R. Redfern, R. F. Butler, *Proc. SPIE* **4876**, in press.
15. J. L. L. Voûte *et al.*, *Astron. Astrophys.* **385**, 733 (2002).
16. T. H. Hankins, *Astrophys. J.* **169**, 487 (1971).
17. Radio propagation through the interstellar medium is subject to a frequency-dependent delay that is proportional to the line-of-sight electron density. This delay can be completely corrected for with the appropriate filter, and in that case it is referred to as coherent dedispersion.
18. The width of the WSRT tied-array fan beam is ~10 arc sec, and the total contribution of the Crab nebula emission to the system temperature is ~120 K.
19. M. Roberts, personal communication.
20. E. M. Standish, *Astron. Astrophys.* **114**, 297 (1982).
21. The beaming fraction describes what fraction of the sky is illuminated by the pulsar during each rotation. It is a reasonable assumption that this fraction will be energy dependent.
22. R. D. Blandford, E. T. Scharlemann, *Mon. Not. R. Astron. Soc.* **174**, 59 (1976).
23. J. Arons, *Space Sci. Rev.* **24**, 437 (1970).
24. T. H. Hankins, J. S. Kern, J. C. Weatherall, J. A. Eilek, *Nature* **422**, 141 (2003).
25. G. F. Rybicki, A. P. Lightman, *Radiative Processes in Astrophysics* (Cambridge Univ. Press, Cambridge, 1979).
26. A. Golden *et al.*, *Astron. Astrophys.* **363**, 617 (2000).
27. We thank Enterprise Ireland for its support under the Basic Grant Research scheme. P.O.C. is grateful for support under the Higher Education Authority (HEA)–funded CosmoGrid project. The WHT is operated on the island of La Palma by the Isaac Newton Group in the Spanish Observatorio del Roque de los Muchachos of the Instituto de Astrofisica de Canarias. The WSRT is operated by ASTRON (Netherlands Foundation for Research in Astronomy) with financial support from the Netherlands Organisation for Scientific Research (NWO). We thank M. Roberts from Jodrell Bank for the provision of the radio ephemeris (JBE), R. Butler for help in the production of this manuscript, and A. Boyle for help during the optical observations.

30,000 Years of Hydrothermal Activity at the Lost City Vent Field

Gretchen L. Früh-Green,[1]* Deborah S. Kelley,[2] Stefano M. Bernasconi,[1] Jeffrey A. Karson,[3] Kristin A. Ludwig,[2] David A. Butterfield,[4] Chiara Boschi,[1] Giora Proskurowski[2]

Strontium, carbon, and oxygen isotope data and radiocarbon ages document at least 30,000 years of hydrothermal activity driven by serpentinization reactions at Lost City. Serpentinization beneath this off-axis field is estimated to occur at a minimum rate of 1.2×10^{-4} cubic kilometers per year. The access of seawater to relatively cool, fresh peridotite, coupled with faulting, volumetric expansion, and mass wasting processes, are crucial to sustain such systems. The amount of heat produced by serpentinization of peridotite massifs, typical of slow and ultraslow spreading environments, has the potential to drive Lost City–type systems for hundreds of thousands, possibly millions, of years.

Mantle peridotites are exposed at shallow structural levels along slow and ultraslow spreading ridges. The discovery of spectacular carbonate towers at the Lost City hydrothermal field (LCHF) has stimulated interest in the role of serpentinization in generating hydrogen- and methane-rich fluids and driving hydrothermal circulation and in the biological communities that may be supported in these environments. The LCHF lies on the Atlantis Massif, a dome-like exposure of serpentinized peridotite at 30°N, ~15 km west of the Mid-Atlantic Ridge axis (*1*). The carbonate-brucite chimneys at the LCHF are up to 60 m high and are the tallest vent structures yet discovered on the sea floor (Fig. 1). In contrast to black smoker systems, the LCHF vents emit diffuse, high-pH (from 9 to 10) fluids at temperatures of 40° to 75°C. Venting is probably sustained primarily by exothermic serpentinization reactions (*1*), and much remains to be learned about the temporal, spatial, and chemical evolution of these systems.

Mixing of seawater and warm vent fluids with elevated hydrogen and methane concentrations derived from serpentinization provide ideal conditions for abundant thermophilic and mesophilic microbial communities within the hydrothermal structures (*1–3*). Such reducing, ultramafic systems may represent analogs to early Earth environments and may provide insights into the require-

[1]Department of Earth Sciences, Eidgenössische Technische Hochschule, Zürich (ETH-Z), CH-8092 Zurich, Switzerland. [2]School of Oceanography, University of Washington, Seattle, WA 98195, USA. [3]Division of Earth and Ocean Sciences, Duke University, Durham, NC 27708–0230, USA. [4]University of Washington and National Oceanographic and Atmospheric Administration–Pacific Marine Environmental Laboratory, Seattle, WA 98195, USA.

*To whom correspondence should be addressed. E-mail: gretli@erdw.ethz.ch

ments for the emergence of life on and within the sea floor (*4−6*).

The LCHF rests on a terrace at a water depth of 750 to 850 m and is underlain by variably altered and deformed ultramafic and mafic rocks [~1.5 million years (My) old] that have been exposed by long-lived detachment faulting (*1, 7–9*). The Atlantis Massif is ~15 to 20 km across, and its southern face is bounded by a major escarpment with >3800 m of relief adjacent to the Atlantis Fracture Zone. At the summit, the basement is dominated by heterogeneously foliated serpentinites, unconformably overlain by polymictic sedimentary breccias and bedded pelagic limestones or chalks that form a flat-lying carbonate cap (Fig. 2). The limestones and matrix of the breccias consist of highly indurated foraminiferal sand with a well-preserved subtropical fauna (fig. S1). The clasts in the breccias are variably deformed and altered and include clusters of hydrothermal minerals and reworked carbonate material. This indicates that hydrothermal activity was nearly contemporaneous with fracturing and that lithification of the pelagic sediments was relatively rapid. Some reworked carbonate fragments have distinct tube-like structures arranged in a subparallel fashion that we interpret as fossilized pathways of diffuse fluids.

Calcite and/or aragonite veins are abundant, and mm- to cm-sized fractures in the basement are filled by fine-grained carbonate sediments and lithic fragments (fig. S1). Veining generally predates sedimentary fracture-infilling. The youngest hydrothermal phases include the LCHF chimneys and carbonate precipitates on outcrop surfaces, in cavities, and as growths protruding from fissures that are locally venting diffuse fluids. Detachment faulting led to the initial exposure of the peridotites and may have provided important fluid pathways during the early evolution of the massif. Fracturing, breccia formation, carbonate precipitation, and active venting are currently controlled by steeply dipping normal and low-angle faults that postdate detachment faulting (Fig. 2).

Active structures consist primarily of white, porous, friable aggregates of aragonite and brucite. The inactive chimneys contain variable proportions of calcite and aragonite with or without brucite. Minor hydrothermal silicate minerals and microfossils are cemented into the vent edifices. They show a wide range of porosity, friability, and internal textures and commonly have complex constructions with overgrowths and cross-cutting veins. The oldest recovered structure is well lithified and contains calcite and Mg-rich calcite (Fig. 1 and Table 1). Differences in mineralogy and porosity may be related to the conversion of aragonite to calcite, the dissolution of brucite, which is undersaturated in
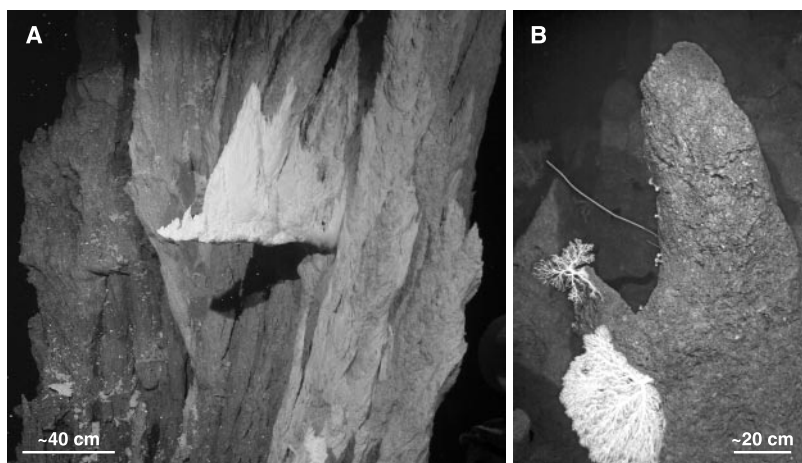

Fig. 1. (**A**) Actively venting flange (55°C) with white, feathery carbonate precipitates on the side of a ~25-m-high structure composed of composite towers in the eastern part of the LCHF. (**B**) Older vent structures are well cemented and have brownish, knobby surfaces that are overgrown with corals.
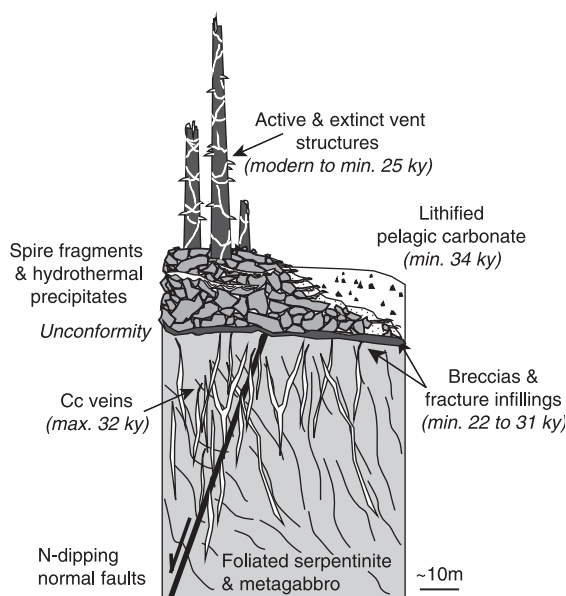

Fig. 2. Relative ^{14}C ages and geologic setting of the LCHF, showing N-S outcrop relationships of the basement to the overlying sedimentary rocks and vent structures. min., minimum; max., maximum; ky, thousand years old.

seawater (*10–12*), and new precipitation of calcite during cementation. Recrystallization and cementation in the presence of seawater is supported by $^{87}Sr/^{86}Sr$ ratios, which change from basement-dominated values of 0.7076 to 0.7079 in the active chimneys toward seawater-like ratios of up to 0.7090 in the inactive structures (Table 1).

Accelerator mass spectrometry (AMS) ^{14}C age-dating indicates that normal faulting, breccia formation, sedimentation, veining, and venting have been broadly contemporaneous and commenced at least 30,000 to 34,000 years ago (Table 1). The ^{14}C ages of the sediments and vents represent minimum ages, because subsequent cementation and recrystallization may have added younger carbon. In contrast, the ages of the calcite veins are considered maximum ages, because C isotope data indicate a nonradiogenic

mantle-carbon component in the fluids. However, in our samples, veining predates brecciation and fracture-infilling, and the veined basement rocks are overlain by lithified sediments. This indicates that the ^{14}C dates of the veins are close to true ages.

Initial hydrothermal flow associated with venting must be older than 25,000 years, the age of our oldest dated vent sample, because many of the structures lie on a 10- to 20-m-high pile of vent debris that is overgrown and cemented by younger precipitates (Fig. 2). Furthermore, fragments that resemble paleo-flow channels are observed in some of the lithified sediments. The actively venting structures give modern ages and indicate that the carbonate ions are derived directly from near-bottom seawater and possibly contain a slight component of bomb radiocarbon (*13*). Sr isotope ratios indicate that the precipita-

Table 1. Isotopic compositions and ^{14}C ages of sedimentary rocks, hydrothermal deposits, and vent fluids at the Atlantis Massif. Depths are reported as meters below sea level. $\delta^{13}C$ and $\delta^{18}O$ values of the carbonate material are in ‰ relative to the Vienna Pee Dee Belemnite standard; $\delta^{18}O$ values of the vent fluid are relative to the Vienna Standard Mean Ocean Water standard (12). AMS ^{14}C ages are conventional radiocarbon ages, uncorrected for reservoir ages. Mineral abbreviations: cc, calcite; arag, aragonite; bru, brucite; T, temperature.

| Sample	Depth	$\delta^{13}C$	$\delta^{18}O$	[14]C Age	AMS ref. no.	$^{87}Sr/^{86}Sr$	Sample details
				Vent samples			
3651-0908B	844	1.4	1.7	25120 ± 210	ETH-26138		Gray extinct chimney; cc, high-Mg cc
3651-0938W	786	1.6	4.5	11820 ± 85	ETH-26139	0.70866	White extinct chimney; arag, cc
3651-0944	785	2.2	3.8	300 ± 35	CAMS-95436	0.70799	Feathery white deposit from fissure; arag, cc, bru
3651-1022	731	1.6	2.2	50 ± 45	ETH-26397	0.70760	Active vent, T = 75°C; white botryoidal deposit; arag, bru
3651-1123	799	2.4	4.5	970 ± 35	CAMS-95437	0.70908	Small pinnacle from talus; arag, minor microfossils
3651-1149	792	2.0	3.9	195 ± 45	ETH-26396	0.70793	Active vent, T = 55°C, friable white material; arag, bru
3651-1231	731	2.4	4.0	585 ± 35	CAMS-95438	0.70896	White porous sample from inactive tower; arag, cc, minor microfossils
				Pelagic limestones, breccias, and infillings			
3641-1549A	1794	1.5	2.9	34100 ± 400	ETH-26401		Fossil-rich, bedded pelagic limestone
3645-1145C	957	2.7	4.6	30930 ± 310	ETH-26399		Carbonate (cc/Mg-rich cc) matrix in basaltic breccia
3648-1534B	947	3.2	5.2	22060 ± 220	ETH-26400		Micritic carbonate in-filling in fractured serpentinite
3648-1545B	920	2.4	1.5	25430 ± 170	CAMS-95435		Carbonate (cc) matrix in sedimentary breccia
3652-1002B	732	2.9	4.7	25120 ± 200	ETH-26398		Micritic carbonate pockets in fractured serpentinite
				Veins			
3648-1424N	1084	−2.3	−14.2	31980 ± 380	ETH-26140		cc veins in fractured gabbro
3652-0905V2	863	−2.8	−16.8	31960 ± 400	ETH-26141		cc veins in highly fractured serpentinite
				Vent fluids			
3651-1013	731		0.1			0.70697	Active vent T = 75°C
3651-1201A	792		0.0			0.70726	Active vent T = 55°C
3651-1201B	792		0.1			0.70745	Active vent T = 55°C
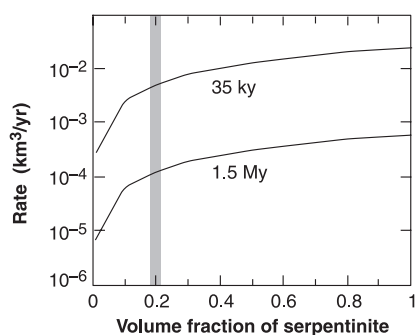
Fig. 3. Time-integrated rates of serpentinization as a function of fraction of serpentinite to unaltered peridotite at the Atlantis Massif, calculated for a 1.5-My and 35-thousand-year alteration history. The calculations assume a total volume of peridotite of 900 km³ and are independent of fluid-flow rates or background heat flow. Shaded area highlights rates predicted for serpentinization of 20% of the volume of peridotite in the massif (SOM Text).

tion of aragonite and brucite in the active vents is triggered by mixing of seawater with the high-pH hydrothermal fluids ($^{87}Sr/^{86}Sr$ = 0.7070 to 0.7075) derived from subsurface serpentinization reactions (Table 1). Because of the limited number of vent samples and a bias in sampling recently active structures, we place no importance on the apparent bimodal distribution of ages. The morphologies of the vent structures imply more or less continuous construction rather than discrete events; however, additional data are required to unequivocally address this.

The ^{14}C ages indicate that many of the sediments sampled to date were deposited just before the last glacial maximum 20,000 years ago. Bulk $\delta^{18}O$ values of 1 to 3 per mil (‰) (Table 1) are consistent with precipitation from ^{18}O-rich waters during glacial times (~1‰ higher than modern Atlantic seawater at 30°N) (14–16). However, many samples have particularly high $\delta^{18}O$ values (>4‰), which indicate precipitation at ambient temperatures from hydrothermal fluids that had strongly interacted with the basement ($\delta^{18}O_{H_2O}$ of >2‰). High $\delta^{13}C$ values of 2 to 3.5‰ in the chimneys and sediments may reflect CO_2 reduction to methane (resulting in heavy residual CO_2 values and light methane values), a process that typically accompanies serpentinization (2, 17). In contrast, veins and bulk carbonate in the basement have $\delta^{13}C$ values as low as −6‰, which suggests a ^{13}C-depleted component, presumably methane, in the deep fluids. Some of these samples have negative $\delta^{18}O$ values that indicate precipitation temperatures of ~50° to 225°C.

In addition to controlling fluid compositions, serpentinization produces significant amounts of heat through exothermic hydration (17–19). We can evaluate serpentinization rates and the consequences for the duration of hydrothermal activity by taking into consideration the age of the lithosphere at the Atlantis Massif, the present volume of serpentinite, and the ^{14}C ages [Supporting Online Material (SOM) Text]. Limits on the time-integrated rate of serpentinization can be made by considering two end-member scenarios: (i) Serpentinization occurred over the entire 1.5-My history of extension and emplacement, and (ii) serpentinization is restricted to ~35,000 years, during which time the LCHF formed (Fig. 3).

On the basis of field and geophysical data (20–21), we estimate that 180 km³ (~20%) of the massif is completely serpentinized and that the south wall consists of 45 km³ of serpentinite (SOM Text). If serpentinization was continuous over 1.5 My, the time-integrated rate of serpentinization is about 1.2×10^{-4} km³/year (Fig. 3), which is slightly higher than previous estimates (19, 22). At this rate, <10% (3 to 4.2 km³) of the south wall of the massif needs to be altered in the 25- to 35-thousand-year history of venting indicated by the ^{14}C ages. Another 6 My would be required to serpentinize the remaining fresh peridotite in the core of the massif. Our second (admittedly unrealistic) scenario

provides an upper limit to the rate of serpentinization and yields a rate of 5.1 × 10^{-3} km³/year (for 20% alteration of the massif). At this rate, it would take another 140,000 years to serpentinize the remaining volume of peridotite.

Independent of the degree of alteration in the Atlantis Massif, these calculations illustrate that the volume of peridotite is not the limiting factor in serpentinization-driven hydrothermal systems. In the absence of substantial conductive cooling, the amount of heat produced by serpentinization has the potential to drive moderate-temperature, Lost City–type systems for hundreds of thousands, if not millions, of years. The rate at which water is able to enter relatively cool mantle rocks (<425°C) (17, 19), linked with tectonic activity, uplift rates, and crack permeabilities, are much more important in limiting the life of such systems. These processes in turn will influence conductive cooling and the efficiency of the system to transport heat released during serpentinization. Ultimately, temperature controls the rate of serpentinization. Rates are likely to be highest at temperatures of ~250°C; hydration and diffusion rates are notably low below 100°C (19, 23).

Our studies indicate that tectonic and hydrothermal processes at the LCHF are intimately linked and that they directly influence fluid-flow paths and the chemical and isotopic evolution of the fluids. Serpentinization and talc-metasomatism are a direct result of mantle denudation and most likely commenced close to the spreading center. Both processes are undoubtedly ongoing below the vent field. As the system evolved, a number of self-propagating mechanisms increased permeability and fluid access that may ultimately be crucial for the formation of such vent fields. For example, along the southern scarps of the massif, complex networks of steeply dipping faults, fracturing, and mass wasting are driven by fracture-zone tectonics and alteration-induced volumetric expansion (1, 9). This enhances exfoliation along the scarp, penetration of seawater into the relatively cool, fresh peridotite, and propagation of the serpentinization front toward the north into the central dome of the massif. In addition, diffusely percolating, high-pH fluids emanating from the underlying serpentinites promote rapid sediment lithification (1, 6), which offers an efficient mechanism for slowing heat loss and maintaining higher temperatures in the basement. Collectively these processes have the potential to prolong hydrothermal activity for tens of thousands of years. If high-pH, reducing, ultramafic systems are analogous to early Earth environments, the LCHF provides a natural laboratory to understand the links between serpentinization, carbonate precipitation, and microbial activity in ancient ecosystems (6).

References and Notes

1. D. S. Kelley *et al.*, *Nature* **412**, 145 (2001).
2. M. E. Berndt, D. E. Allen, W. E. Seyfried Jr., *Geology* **24**, 351 (1996).
3. M. O. Schrenk, P. Cimino, D. S. Kelley, J. A. Baross, *Eos* **83**, F2301 (abstr. B71B-0742) (2002).
4. G. MacLeod, C. McKeown, A. J. Hall, M. J. Russell, *Orig. Life Evol. Biosph.* **23**, 19 (1994).
5. E. L. Shock, M. D. Schulte, *J. Geophys. Res.* **103**, 28513 (1998).
6. D. S. Kelley, J. A. Baross, G. L. Früh-Green, M. O. Schrenk, J. A. Karson, *Eos.* **83**, F222 (abstr. B62A-03) (2002).
7. D. K. Blackman, J. R. Cann, B. Janssen, D. K. Smith, *J. Geophys. Res.* **103**, 21315 (1998).
8. J. R. Cann *et al.*, *Nature* **385**, 329 (1997).
9. D. K. Blackman *et al.*, *InterRidge News* **10.1**, 33 (2001); available online at http://triton.ori.utokyo.ac.jp/~intridge/irn-toc01.htm#101.
10. Thermodynamic calculations with the program PHREEQE (*12*) indicate that seawater is undersaturated with respect to brucite, in contrast to supersaturation of brucite, talc, and serpentine for mixing of seawater with the range of vent fluid compositions reported by (*1*).
11. D. L. Parkhurst, D. C. Thorstenson, L. N. Plummer, *U.S. Geological Survey Water-Resources Investigations Report 80-96* (1980).
12. Materials and methods are available as supporting material on *Science* Online.
13. 1973 GEOSECS ¹⁴C data for Station 117, the closest to LCHF, indicate Δ¹⁴C values of −32.2 and −67.9 at depths of 686 and 1076, respectively, and correspond to reservoir ages of 268 and 565 years, respectively. The young ages of the active vents suggest that bomb radiocarbon has penetrated deeper into the water column and that the vents must be fed by relatively shallow water masses. If recharge of the hydrothermal system was deep water, ages of at least 830 years (reservoir age at ~30°N) would be obtained. More information can be found online at http://iridl.ldeo.columbia.edu/SOURCES/GEOSECS/.
14. L. D. Stott, C. M. Tang, *Paleooceanography* **11**, 37 (1996).
15. G. S. Schmidt, G. R. Bigg, E. J. Rohling, Global Seawater Oxygen-18 Database (1999); available online at www.giss.nasa.gov/data/o18data/.
16. D. P. Schrag *et al.*, *Quat. Sci. Rev.* **21**, 331 (2002).
17. G. L. Früh-Green, J. A. D. Connolly, A. Plas, D. S. Kelley, B. Grobéty, in *The Subseafloor Biosphere at Mid-Ocean Ridges*, W. D. Wilcock, D. S. Kelley, E. DeLong, C. Cary, Eds. (American Geophysical Union, Washington, DC, in press).
18. W. S. Fyfe, P. Lonsdale, in *The Sea*, C. Emiliani, Ed. (Wiley, New York, 1981), vol. 7, pp. 589–638.
19. A. H. Macdonald, W. S. Fyfe, *Tectonophysics* **116**, 123 (1985).
20. R. S. Detrick, J. A. Collins, *Eos* **79**, F800 (1998).
21. S. L. Nooner, G. S. Sasagawa, D. K. Blackman, M. A. Zumberge, *Geophys. Res. Lett.* **30**, 1446 (2003).
22. R. P. Lowell, P. A. Rona, *Geophys. Res. Lett.* **29**, 10.1029/2001GL01411 (2002).
23. B. Martin, W. S. Fyfe, *Chem. Geol.* **6**, 185 (1970).
25. We thank I. Hajdas (ETH) and T. Brown [Center for Accelerator Mass Spectrometry (CAMS)] for ¹⁴C-age dating, E. William for evaluation of sea-floor imagery, and B. Nelson for Sr measurements. We acknowledge funding from ETH grant 0-20890-01 to G.L.F.-G. and from NSF grants OCE97-12549 to D.S.K. and OCE97-12430 to J.A.K. G.P. was in part supported by NSF and the CAMS at Lawrence Livermore National Laboratory through the University Collaborative Research Program.

First-Principles Calculations of PuO$_{2\pm x}$

L. Petit,[1,2] A. Svane,[1]* Z. Szotek,[3] W. M. Temmerman[3]

The electronic structure of PuO$_{2+x}$ was studied using first-principles quantum mechanics, realized with the self-interaction corrected local spin density method. In the stoichiometric PuO$_2$ compound, Pu occurs in the Pu(IV) oxidation state, corresponding to a localized f⁴ shell. If oxygen is introduced onto the octahedral interstitial site, the nearby Pu atoms turn into Pu(V) (f³) by transferring electrons to the oxygen. Oxygen vacancies cause Pu(III) (f⁵) to form by taking up electrons released by oxygen. At $T = 0$, the PuO$_2$ compound is stable with respect to free oxygen, but the delicate energy balance suggests the possible deterioration of the material during long-term storage.

Although Pu oxidizes readily, until recently it was accepted wisdom that PuO$_2$ is the chemically stable Pu oxide (*1*); showing no sign of reaction when exposed to air, it was the compound of choice for the long-term storage of Pu. The discovery by Haschke *et al.* (*2*) of higher composition binary oxides, PuO$_{2+x}$ (x ≤ 0.27), might therefore have wide-ranging implications (*3,4*). The oxidation reaction was found to occur in the presence of water, PuO$_2$ + xH$_2$O → PuO$_{2+x}$ + xH$_2$, at temperatures in the range of 25° to 350°C. Nevertheless, despite considerable experimental evidence, the existence of PuO$_{2+x}$ remains controversial (*5*), because many earlier attempts to prepare oxides containing Pu atoms with oxidation states above 4 have failed.

We studied changes in the Pu f-electron configuration induced by the oxidation/reduction process from PuO$_2$ to PuO$_{2+x}$/PuO$_{2-x}$, based on ab initio electronic structure

¹Department of Physics and Astronomy, University of Aarhus, DK-8000 Aarhus C, Denmark. ²Computer Science and Mathematics Division, and Center for Computational Sciences, Oak Ridge National Laboratory, Oak Ridge, TN 37831–6114, USA. ³Daresbury Laboratory, Daresbury, Warrington WA4 4AD, UK

*To whom correspondence should be addressed. E-mail: svane@phys.au.dk